Sensors and Actuators: A. Physical 332 (2021) 113071

Contents lists available at ScienceDirect

Sensors and Actuators: A. Physical

journal homepage: www.elsevier.com/locate/sna

Fiber optic tactile sensor for surface roughness recognition by machine learning algorithms

Serkan Keser, Şekip Esat Hayber*

Department of Electrical-Electronic Engineering, Kırşehir Ahi Evran University, Kırşehir 40100, Turkey

ARTICLE INFO

Article history:
Received 19 April 2021
Received in revised form 31 August 2021
Accepted 1 September 2021
Available online 4 September 2021

Keywords:
Fiber optic tactile sensor
Interferometry
Surface roughness recognition
DWT
SVM
KNN

ABSTRACT

In this study, a sensor tip with a metallic hemispherical nozzle tip (MHNT) design based on the Fabry-Perot interferometer was developed for surface roughness recognition (SRR). Sandpaper samples with ten different arithmetical mean deviations of the surface (S_a) values were used as surfaces to be recognized. The feature vectors were found by applying the discrete wavelet transform (DWT) to the analog signals obtained from the sandpaper samples. Machine learning (ML) algorithms K-nearest neighbor (KNN) and support vector machine (SVM) were used for classification. An in-depth recognition process was carried out using the classifiers' different length criteria and kernel types. In the test process, each category consists of two sub-categories as testing within the training dataset (TWITD) and testing without the training dataset (TWOTD). The experiments were carried out in a controlled manner with the conveyor belt system (CBS) and manual. As a result of the experimental studies, the average recognition rates (R_{ave}) for CBS were found as 84.2% and 81.6% for TWITD and TWOTD, while the R_{ave} for the manual are found as 80% and 77.5% for TWITD and TWOTD, respectively.

1. Introduction

With the development of technology, the perception of object surfaces' various features has started to gain significant importance [1–8]. It is crucial that characteristics such as the roughness and hardness of the object's surfaces can be perceived similarly to human perception. Thus, system behaviors can be determined based on object properties. Commonly used tactile sensors are transducers that interact directly with the surface through physical contact [7,9]. Tactile sensors have been inspired by human touch. The use of tactile sensors is increasing day by day, especially in healthcare and robotic applications [10]. The most widely used tactile sensor technologies in robotics are based on capacitive [11], piezoresistive [12], optical [2,3,13], magnetic [14], and piezoelectric [15] methods. Various robotic systems have been developed using tactile sensor technologies at the robot hand and fingertip [8,16]. For example, the hand of the humanoid iCub robot [10] equipped with piezoelectric sensors performs functions such as squeezing, pushing, and touching the objects, allowing the texture, hardness, and shape of the object to be perceived. Piezoelectric sensors generate an electrical signal proportional to the applied force or pressure. They are suitable for measuring vibrations and are also widely used because of their sensitivity and high-frequency response [11]. As a piezoelectric sensor material, polyvinylidene fluoride (PVDF) is the most widely used material in tactile sensors' production due to its flexibility, machinability, and chemical stability [5]. Despite all these advantages, they have some problems when exposed to heavy environments because of their low resistance to chemicals and high temperatures and are affected by electromagnetic interference. These systems consist of many electronic components and electrical cabling, which can weaken the electronic signals much. This situation makes them less useful in many conditions.

One of the essential uses of tactile sensors is surface roughness recognition (SRR) [15,17–19]. Besides, optical sensors developed for SRR are available in the literature [13,20]. On the other hand, fiber optic tactile sensors, which are a branch of optical sensors, can be used as contact [9,21–24] and non-contact [25–27] with the object. Although non-contact sensing surface reflectivity becomes important, this may not produce successful results for all surfaces. Fiber Bragg grating (FBG)s, an interferometric structure, have a prominent place among the tactile sensors [28–32]. Fabry-Perot, another important interferometric structure, was used in tactile sensors but not for surface roughness recognition [33–36].

The fiber optic tactile sensor, which is based on the Fabry-Perot interferometer principle that allows a functional single-point

---

* Corresponding author.
E-mail addresses: skeser@ahievran.edu.tr (S. Keser), sehayber@ahievran.edu.tr (Ş.E. Hayber).

https://doi.org/10.1016/j.sna.2021.113071

detection structure and enables SRR, is the subject of this study. Firstly, a metallic hemispherical nozzle tip (MHNT) contacting the surface on a metal diaphragm is designed and produced. Then, sandpaper samples with ten various S_a in the same brand, model, and standard were used to obtain signals belonging to various surfaces. The sensor tip is contacted to the object in two ways: a conveyor belt system (CBS) or manually. Then, signals are obtained for each different surface. The discrete wavelet transform (DWT) method is used to generate the feature vectors of these signals. The training dataset is created with feature vectors belonging to each surface class. In the test phase, the feature vectors of the test signals obtained by DWT are classified using machine learning (ML) algorithms K-nearest neighbors (KNN) and support vector machine (SVM). The testing process has been carried out primarily in two categories as CBS and manual. Each category consists of two subcategories as testing within the training dataset (TWITD) and testing without the training dataset (TWOTD). In other words, samples of the training dataset are used in the TWITD, but the TWOTD is that the samples are used outside of the training dataset. The feature vectors were obtained in two different ways with DWT as “coif4” and “daub4”. Two different classifiers are used, KNN and SVM, which are well-known ML algorithms in the literature. In this study, a total of 16 different categories have been tested. The results obtained show that the SRR results vary between 66.2% and 84.2%.

2. Materials and methods

2.1. Design and manufacture of the sensing tip

A prominent member of the interferometric sensor family is the Fabry-Perot interferometer. Many sensors have been produced in the literature with this structure, which is pressure, vibration, refractive index, temperature, etc., can be reproduced. The functionality of the design has also yielded successful results in single-ended point measurement systems. The first interface is fiber-air in the structure with two parallel surfaces, while the second is air-diaphragm. Usually, the diaphragm interface interacts with the sensing medium. These structures are either in direct contact with the sensing zone or, as in acoustic pressure sensors, vibrate due to the acoustic pressure wave’s effect without contact and modulating the interferometer’s optical wave. In our study, the diaphragm structure raised outwards in the form of a hemispherical nozzle is in contact with the surface. Depending on the surface roughness, the vibrating tip causes the optical path, L of the light beam exposed to multiple reflections between two parallel surfaces to change. Depending on the optical path’s change, the optical phase is given in Eq. (1) [37]. λ represents the wavelength of the light source.

$$\phi = \frac{4\pi n_m L}{\lambda} \tag{1}$$

Where n_m, n_f, and n_d represent the Fabry-Perot cavity’s refractive indices, the fiber core, and the diaphragm’s inner surface, respectively. Therefore, the reflectance R_1 and R_2 of the first and second interfaces can be calculated by Eqs. (2) and (3), respectively [38]. The extinction coefficient, κ can be simplified because it is very close to zero in dielectric materials. The situation changes when the surface to which the light wave will interact is metal and should be used in the most general form [39].

$$R_1 = \left| \frac{(n_f - n_m)^2 + \kappa_m^2}{(n_f + n_m)^2 + \kappa_m^2} \right| \tag{2}$$

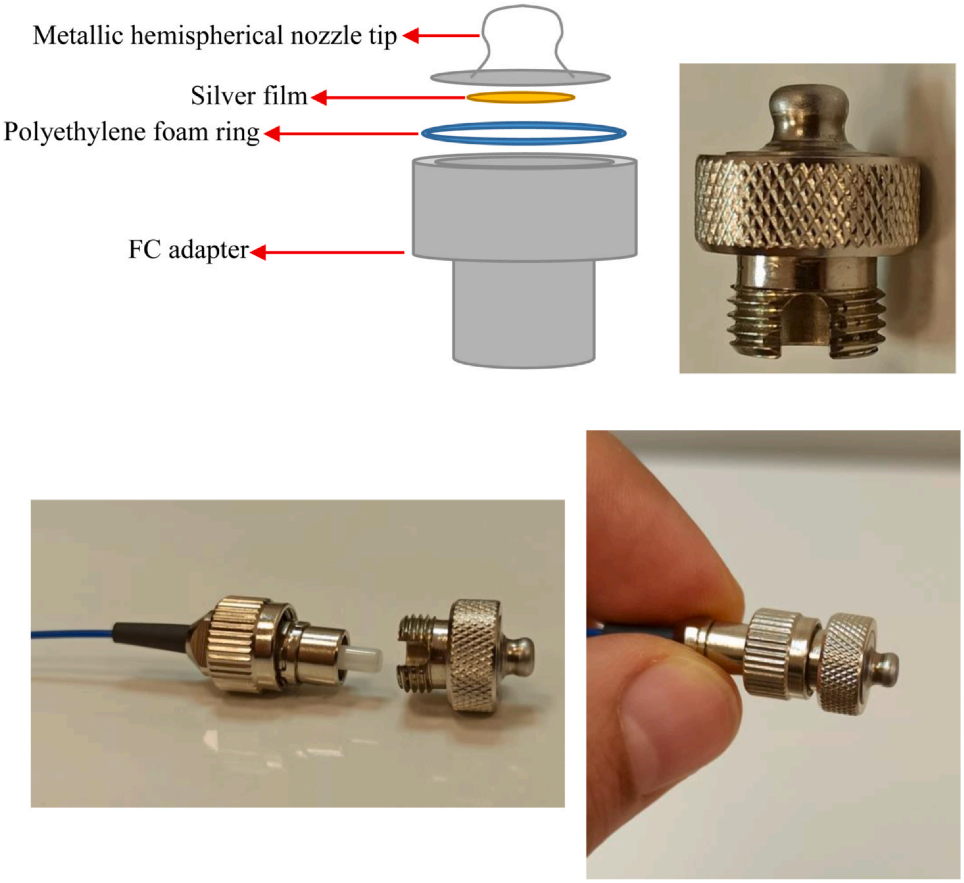

Fig. 1. MHNT assembling stage.

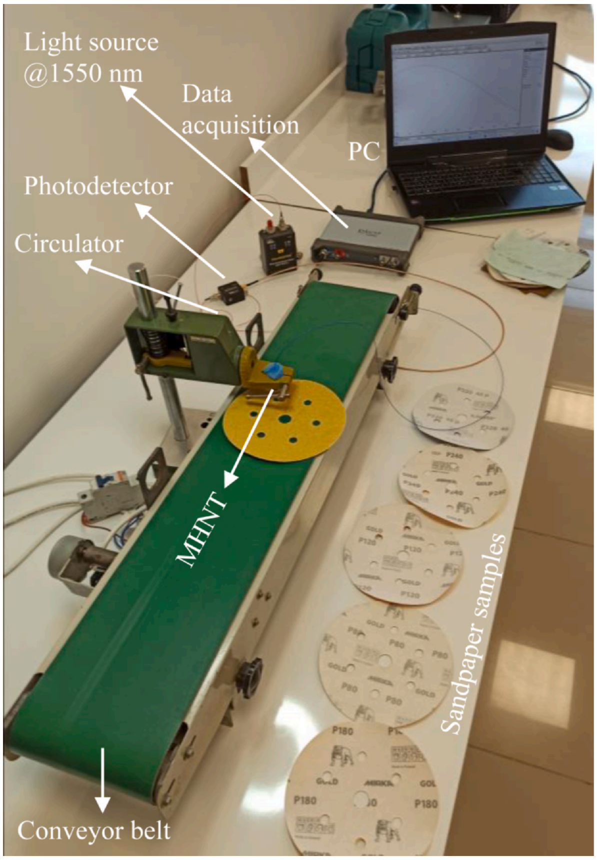

Fig. 2. The schematic diagram of the experimental setup for the SRR system.

κ_m and κ_d are the extinction coefficients of the air and diaphragm surface, respectively.

$$R_2 = \left| \frac{(n_m - n_d)^2 + \kappa_d^2}{(n_m + n_d)^2 + \kappa_d^2} \right| \tag{3}$$

It is given with Eq. (4) to show the optical light intensity, I_r reflected from the interferometer.

$$I_r(L, \lambda) = \alpha_0 I_0(\lambda) \frac{R_1 + \eta R_2 - 2\sqrt{\eta R_1 R_2} cos\phi}{1 + \eta R_1 R_2 - 2\sqrt{\eta R_1 R_2} cos\phi} \tag{4}$$

Where α_0 is optical losses in the system and I_0 is input optical density. Finally, in Eq. (4), the transmission coefficient η of the Fabry-Perot cavity is calculated as in Eq. (5) [40]. w shows the spot size value of the fiber.

$$\eta = \frac{1}{1 + \left(\frac{L\lambda}{\pi n_m w^2} \right)^2} \tag{5}$$

While R_1 generally has typical values for the reflectance in Eqs (2) and (3), R_2 varies according to the diaphragm material. The refractive index of the fiber core in our study is $n_f = 1.4682$, the inner surface of the diaphragm is covered with a silver layer and has values of $n_d = 0.2654$, $\kappa_d = 11.241$ @ 1550 nm [41]. Since $n_m = 1$ and $\kappa_m = 0$, $R_1 = 3.60\%$, $R_2 = 99.17\%$. 96.4% of the optical intensity coming out of the fiber passes into the air medium and reaches the diaphragm's surface. 99.17% of the light rays reaching the diaphragm are reflected (95.60%) and return to the air-fiber interface. Finally, 96.4% of the remaining light rays re-enter the fiber (92.16%).

As can be understood from Eq. (4), the optical intensity at the output will vary depending on the L length change when all parameters are kept constant. In this study, the interferometer's second reflective surface has a metallic hemispherical nozzle tip (MHNT) design. As a result of the MHNT's contact with the rough surface, the L length changes. The sensor tip assembling is shown in stage Fig. 1. MHNT is designed per the standard FC adapter. A silver plate is affixed to the inner surface of the MHNT, which has a radius of 4 mm. It is then fixed to the FC adapter with a polyethylene foam ring to provide elasticity. The sensor type obtained has been developed for fiber terminating with any standard FC/PC connector.

The SRR system consists of the MHNT (Fig. 1), includes a laser @ 1550 nm, the optic circulator (1525–1610 nm SMF with FC/PC), a high-speed photodetector (fiber-coupled InGaAs biased), PC oscilloscope-data logger (Picoscope), constant speed CBS, and PC. All components are shown in Fig. 2.

2.2. Surface roughness recognition (SRR)

This section primarily includes obtaining feature vectors from signals belonging to sandpaper surfaces. Then, the process of recognizing the surface classes with the classifiers used was carried out. The stability of the property vectors belonging to the classes in the training dataset was tested by applying K-fold cross-validation to these vectors. The correct recognition of the surface roughness of the objects depends on the feature vectors obtained from the signals and on the classifiers that can distinguish them well. In general, in the literature, DWT is frequently used to obtain feature vectors in surface roughness studies. It is seen that it gives successful results [42–44]. As classifiers, KNN and SVM algorithms, which are known to provide good results, come to the fore [17,45]. Details of these will be discussed below.

2.2.1. Feature extraction

The studies in the literature show that the frequency information of the signals obtained due to friction gives information about the

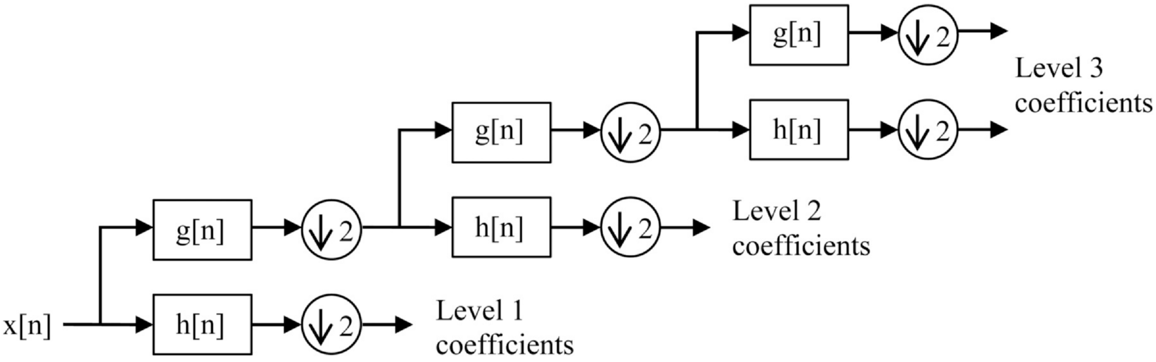

Fig. 3. A 3-level filter bank.

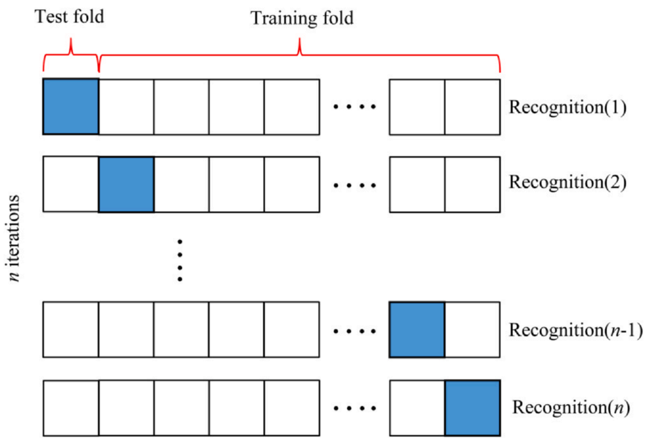

Fig. 4. *K*-fold scheme.

surface roughness [46]. DWT provides a good resolution of the signal in both frequency and time domain [42,47,48]. The signals obtained from the decomposition into different frequency bands using DWT provide satisfactory results in the SRR studies. Thus, feature vectors based on both frequency and time domain can be obtained after transforming signals using DTW [19]. In DWT, each signal is represented by an orthogonal function. The DWT of a signal is calculated by applying low and high pass filters to the signal [49]. The filtering process applied to the signals is given by Eqs. (6) and (7) as the detail and approximation coefficients, respectively [50].

$$d^j[n] = \sum_{i=0}^{r-1} h[i] \times a^{j-1}[2n - i] \tag{6}$$

$$a^j[n] = \sum_{i=0}^{r-1} g[i] \times a^{j-1}[2n - i] \tag{7}$$

Where r and j are the order of filter, the detail coefficients d^j [n] and the approximation coefficients a^j [n] of level j, respectively. $g[i]$ is low pass filter coefficients, $h[i]$ is high pass filter coefficients.

A 3-level DWT filter bank structure is given in Fig. 3.

This separation is repeated, increasing the frequency resolution. While the coefficients corresponding to high frequencies are detail coefficients, the coefficients corresponding to low frequencies are approximate. First, the downsampled version of approximate coefficients is found, and then high and low pass filters are applied to the signal obtained as a result of this downsampling process [49]. Then these processes are repeated for each level.

The wavelet coefficients of an $x(t)$ signal are given by Eq. (8) [49].

$$\gamma_{jk} = \int_{-\infty}^{\infty} x(t) \frac{1}{\sqrt{2^j}} \psi\left(\frac{t - s2^j}{2^j}\right) dt \tag{8}$$

Where j is the scale parameter, and s is the shift parameter. Both are integers. DWT has wavelets such as Haar, Daubechies, Coiflet, and Legendre [49]. Daubechies and Coiflet wavelets were used in this study.

2.2.2. Machine learning algorithms

In the study, the classification model was chosen according to the problem. The KNN and SVM, which are frequently used ML algorithms for roughness recognition in the literature, have been used [15,17,50,51]. KNN algorithm makes classification estimation based on two fundamental concepts [52]. The first is to determine the number of neighbors, and the second is to choose which one to use among the distance criteria (such as Minkowski, Euclidean, city block, and Chebyshev). The test signal is assigned to the most probable class calculated by the nearest neighbor algorithm [53]. City block, one of the distance measures used by KNN, is a distance measure that finds the sum of the absolute values of the differences between two vectors [54]. The city block distance, which is always higher than or equal to zero, is given by Eq. (9).

$$\sum_{i=1}^{u} |a_i - b_i| \tag{9}$$

Where u is the number of vector samples. Another length criterion, Minkowski, is given in Eq. (10) for vectors a and b.

$$\left(\sum_{i=1}^{u} (a_i - b_i)^p\right)^{1/p} \tag{10}$$

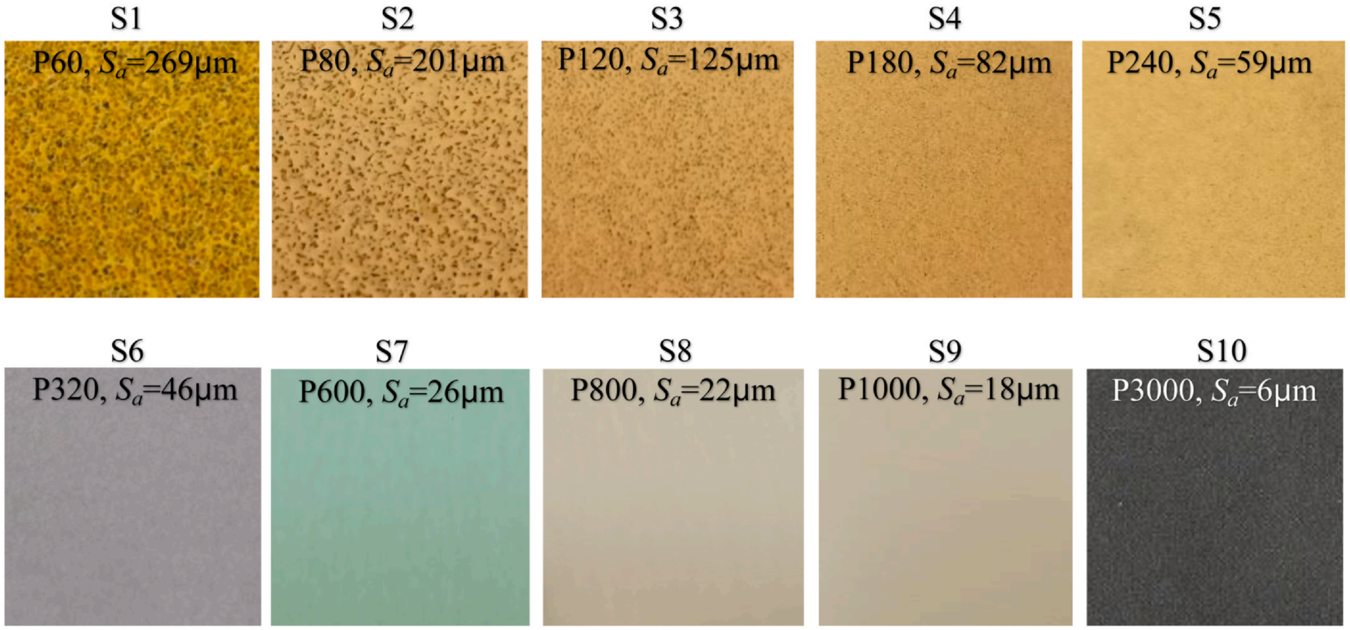

Fig. 5. Sandpaper samples with different S_a values.

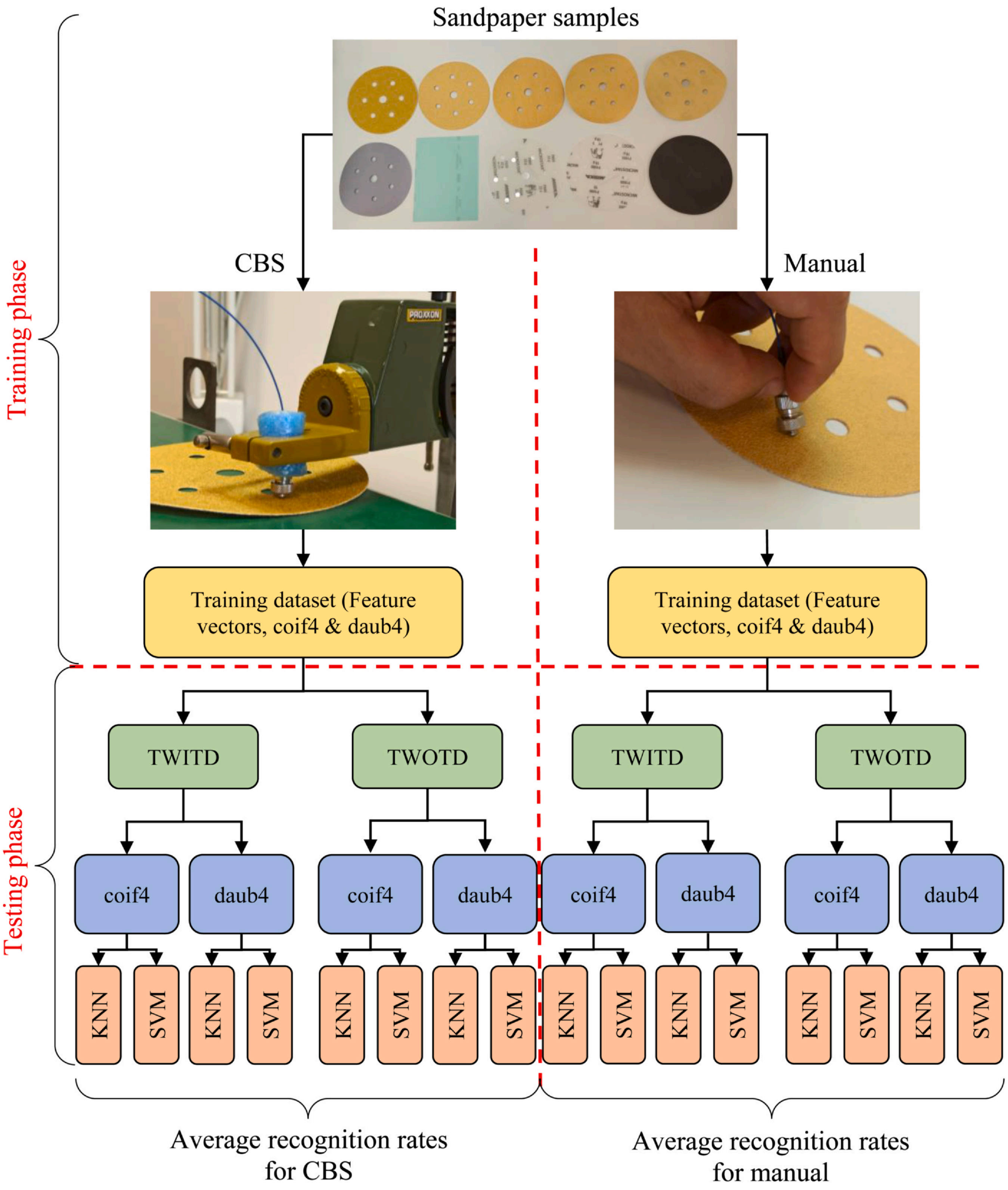

Fig. 6. Scope of the study.

Where p has real values varying between 1 and 2. It corresponds to the Manhattan length criterion for $p = 1$ and the Euclidean length criterion for $p = 2$ [54]. Minkowski, Euclidean, and city block were preferred in our experimental study. Also, the test signals are classified according to the nearest neighborhood of $k = 1$, 3, and 5.

Another classifier, SVM, is a method that can be used for both regression and classification, but mainly in classification problems [55]. Initially, SVM was used to distinguish between two classes and later expanded to achieve multi-class classification [56]. If there are many classes, one of the three approaches is preferred. The first one

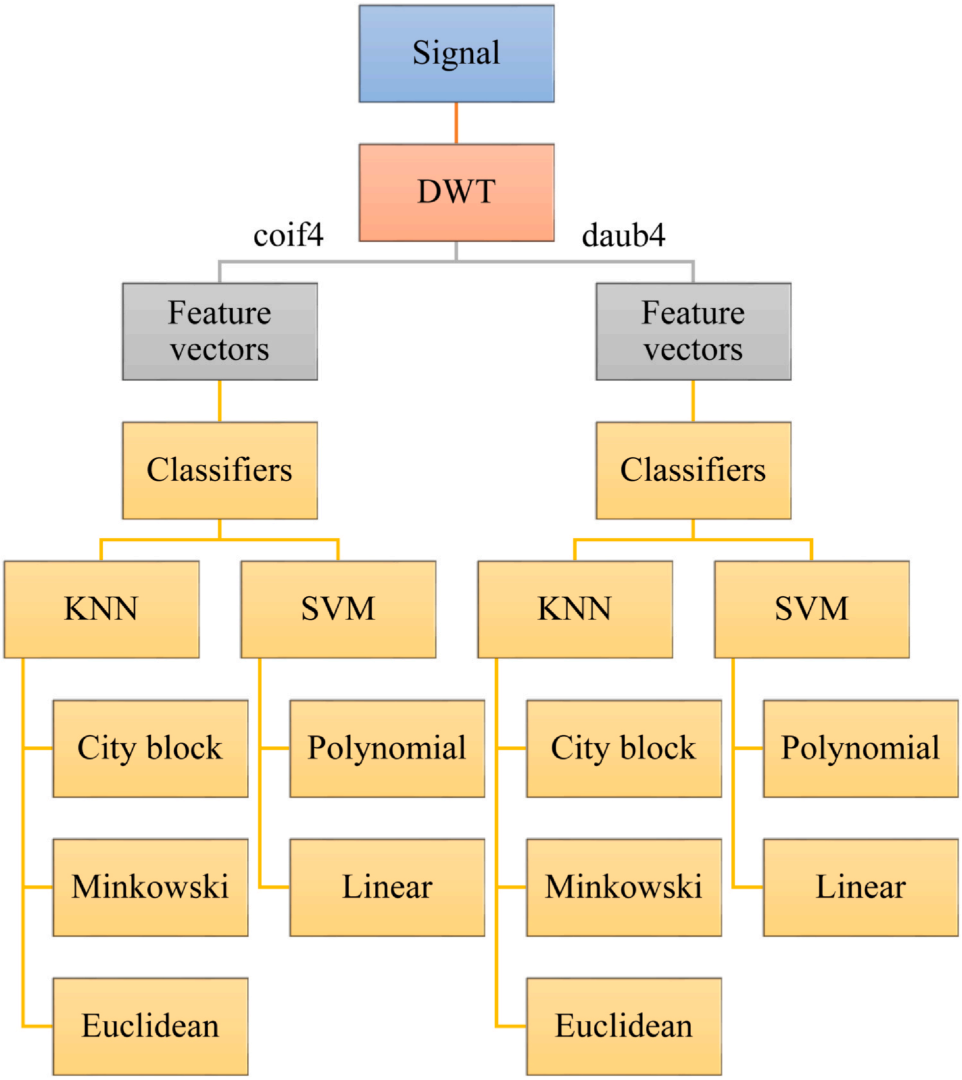

Fig. 7. Block diagram of feature extraction and classifiers.

is reducing the problem to two groups (one-vs-one), the other one is modeling the problem from one group to all groups (one-vs-rest), and the last one is the multi-class ranking approach. The One-vs-rest approach was used in the study. Generally, polynomial, linear, and radial-based kernel functions are used for classification with SVM. In this study, polynomial and linear kernel functions are used.

2.2.3. *K*-fold

The *K*-folds cross-validation method provides meaningful information about the fit of the created recognition system. With this method, training and test sets can be designed flexibly. In *K*-fold cross-validation, the data is divided into different n subsets. n-1 subset is used as train data. An average recognition value is obtained by using n iterations. The *K*-fold scheme is shown in Fig. 4.

An average recognition rate for the jth class is found as follows.

$$R_{ave}^{j} = \frac{1}{n}\sum_{i=1}^{n} R(i), \quad j = 1, 2, \ldots, M \tag{11}$$

$R(i)$ indicates the ith recognition rate, M denotes the total number of classes, and n is number of the iteration. The average recognition rate, R_{ave} for all classes is found as follows.

$$R_{ave} = \frac{1}{M}\sum_{j=1}^{M} R_{ave}^{j} \tag{12}$$

3. Experimental results and discussion

The experimentally used objects in the study consist of sandpaper samples with different roughness levels. Different grit sizes are used for various usage purposes of sandpaper. While producing abrasives with these sizes, standards such as the Federation of European Producers of Abrasives (FEPA), American National Standards Institute (ANSI), Japanese Industrial Standard (JIS), and a Russian classification (GOST) are used. In this study, ten different sandpaper (P60, P80, P120, P180, P240, P320, P600, P800, P1000, and P3000) with macro and micro grain sizes in FEPA standard was used. The arithmetical mean deviation of the surface, $S_{a,}$ is used as the measure of surface roughness of the abrasives. S_a is the most used roughness characterization indicator that describes surface roughness in the vertical direction [57]. The S_a is defined by Eq. (13) [18].

$$S_a = \frac{1}{A}\iint_{A} |z(x, y)|\, dxdy \tag{13}$$

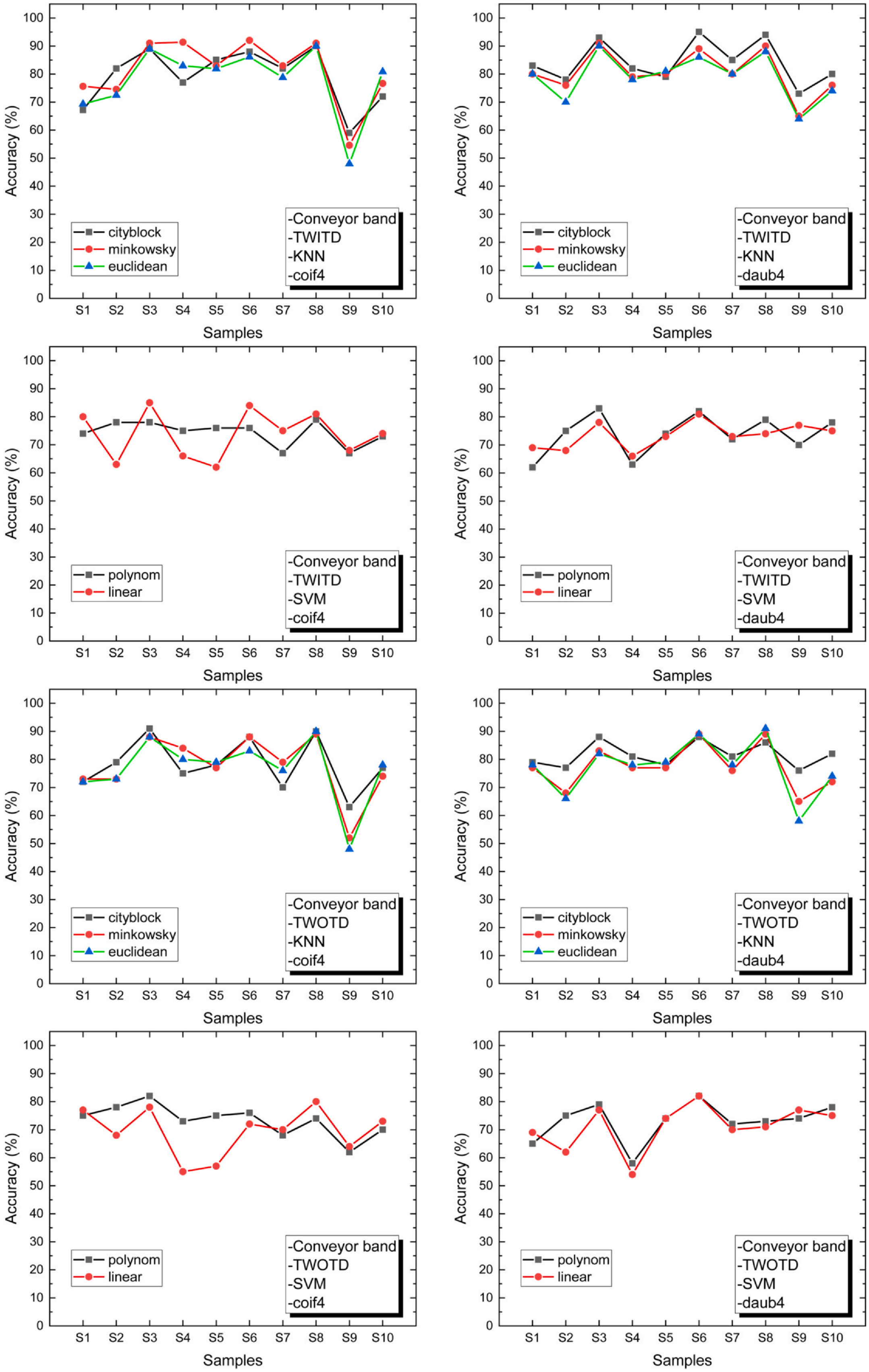

Fig. 8. The CBS test results.

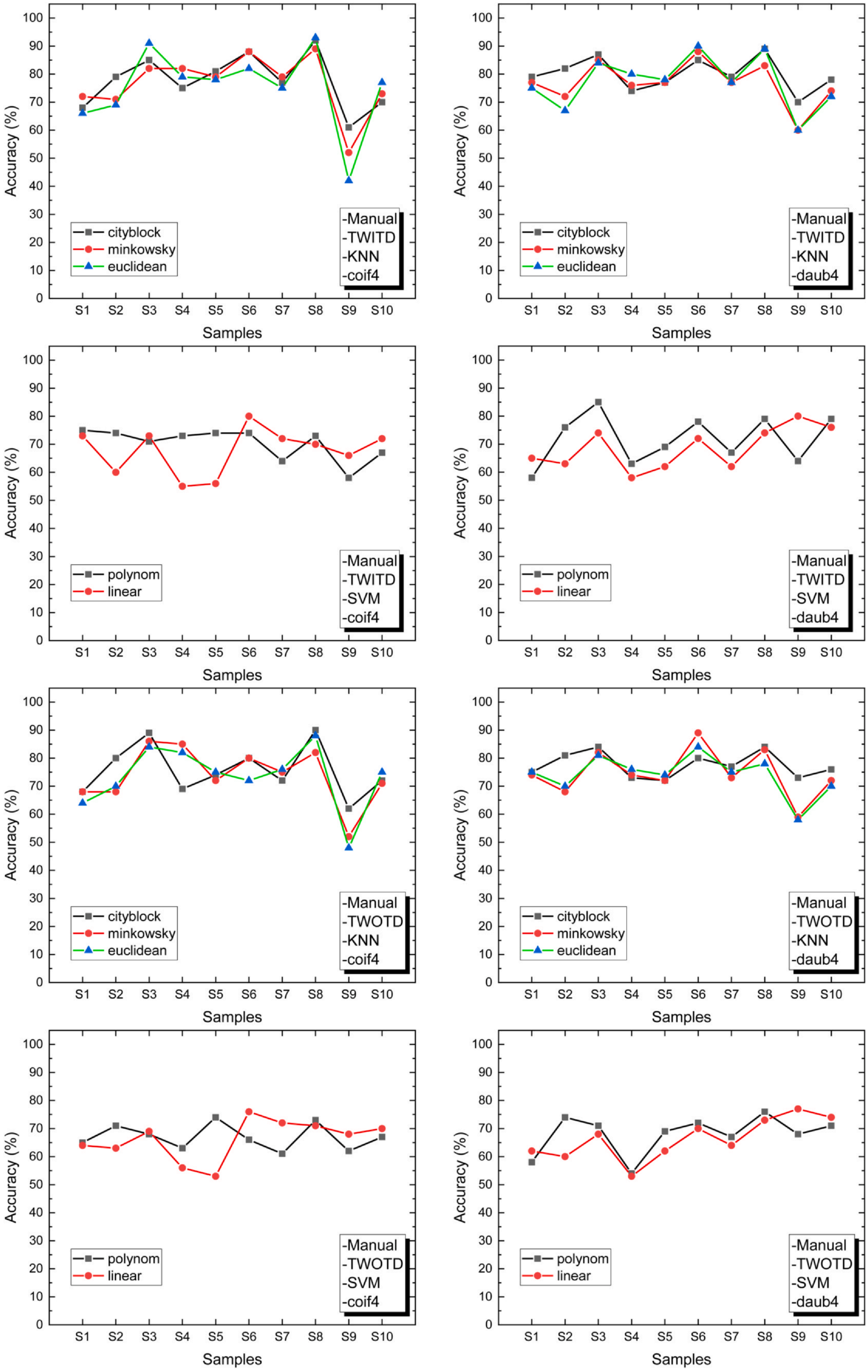

Fig. 9. Manual test results.

Where A is the sandpaper surface area, the limits of the sandpaper's measuring areas are x and y. $z\ (x,y)$ is the height function of the sandpaper surface. FEPA and corresponding S_a values of the images of the sandpaper samples used in the experiment are given in Fig. 5.

The experiment consists of different stages. These stages are shown schematically in Fig. 6. The figure's left column represents the CBS stages, and the right column represents the same stages manually. The CBS has a mechanism that runs at a constant speed. This structure can apply a more stable force and a constant speed to the sanding surfaces than the manual.

On the other hand, in the manual experiment, the friction speed and the applied force may vary more than the CBS. By applying DWT, whose coif4 and daub4 wavelets are used, feature vectors are obtained to create a training data set to the signals obtained from surfaces. Then, the test signals are classified with the classifiers KNN and SVM suitable for this problem. Here, two approaches are used for the testing process. These approaches are called testing within training dataset (TWITD) and testing without training dataset (TWOTD). Thus, a total of 16 different categories were tested in the study.

3.1. Feature extraction and classifiers

The sampling rate of the analog signals generated by shifting the MHNT on the sandpaper surfaces is 20 kHz. Each signal was received at 1.5 s intervals by adjusting the conveyor belt's speed to approximately 0.01 m/s. Each signal is equal to 1.4 s (28,000 samples) by discarding the unwanted parts at the beginning and the end of the signal. In this way, 100 signals were obtained for each sanding surface. It is known that the frequency components of these signals obtained by sliding play a critical role [19]. DWT based on an orthonormal wavelet is used to separate the signals into components [58–60].

For manual and CBS, a training dataset was created by sliding the MHNT 100 times on the sanding surfaces. While using the training dataset signals for TWITD, the friction process was repeated 100 times for TWOTD. In this article, the wavelet functions applied are Daubechies and Coiflets. A total of four layers have been created. A total of 8 components have been used as an approximation component and a detail component in each layer for a signal. Statistical properties in both frequency and time domain have been determined for each component. These properties are used as feature vectors. These statistical properties have been defined as mean, standard deviation, energy, and kurtosis (KT). N represents the signal dimensional and is equal to 28,000 in this study. For each N-dimensional signal, a 64-dimensional feature vector obtained from 32-frequencies and the 32-time domain have been created. For each class, 100 feature vectors, each of which has 64-dimensions, have been obtained.

Two different ML algorithms KNN and SVM were used for classification. The training phase was completed by using the obtained feature vectors and these classifiers. In the test phase, test signals are assigned to the most probable class. The recognition system used in the study is given in Fig. 7. As can be seen from the figure, the feature vectors of the signal were obtained using coif4 and doup4 wavelets of DWT. Then, classification was performed for these feature vectors using KNN, different distance criteria (Minkowski, Euclidean, city block), and various neighbor values ($k = 1$, 3, and 5). It was seen in experimental studies that the best results were obtained for $k = 5$. For SVM, the classification was carried out using polynomial and linear kernel functions. This classification was carried out in two different categories as TWITD and TWOTD.

3.2. The results of surface roughness recognition (SRR)

Recognition performances of the proposed system are given as CBS and manual, respectively, in Fig. 8 and 9. For TWITD, 100-fold cross-validation has been applied. The recognition rates obtained with CBS are shown in the graphs in Fig. 8. These graphs include the analyzes made based on the cases of TWITD-TWOTD, daub4-coif4, KNN-SVM. While applying KNN, recognition rates were examined using three distance measure criteria, Minkowski, Euclidean, and city block. Similarly, recognition rates were found in SVM using polynomial and linear kernel functions. For KNN, the $k = 5$ value, which gives the best result, is shown in the graphs by performing the recognition process based on the nearest neighborhood values of $k = 1$, 3, and 5. Fig. 8 shows that the highest recognition rate was 84.2% (TWITD, daub4, KNN, and city block). After that, 81.6% and 81.27% were obtained (TWOTD, daub4, KNN, and city block) and (TWITD, coif4, KNN, and Minkowski) respectively. The lowest value was obtained with (TWOTD, daub4, SVM, and linear) as 71.1%. Similarly, the experimental study results, which are performed manually, are shown in the graphs in Fig. 9. The top three most successful recognition rates for Manual are (TWITD, daub4, KNN, and city block), (TWITD, coif4, KNN, and city block), and (TWOTD, daub4, KNN, and city block), respectively, 80%, 77.6%, and 77.5%.

When we look at the most general recognition rate averages, it has been determined that the recognition results made with CBS have higher values than manual. This result is expected due to the more controlled operation of CBS than manual. However, the difference in recognition rate performances between CBS and manual is not very high, as seen from Tables 1 and 2. There is no significant

Table 1
SRR average rates for CBS.

	coif4					daub4				
	KNN			SVM		KNN			SVM	
	City block	Minkowski	Euclidean	Polynomial	Linear	City block	Minkowski	Euclidean	Polynomial	Linear
TWITD	79.13	81.27	77.93	74.3	73.8	84.2	80.6	79.1	73.8	73.4
TWOTD	78.3	77.7	76.7	73.3	68.56	81.6	77.3	77.3	73	71.1

Table 2
SRR average rates for manual.

	coif4					daub4				
	KNN			SVM		KNN			SVM	
	City block	Minkowski	Euclidean	Polynomial	Linear	City block	Minkowski	Euclidean	Polynomial	Linear
TWITD	77.6	76.7	75.2	70.3	67.7	80	76.9	77.2	71.8	68.6
TWOTD	75.6	73.9	73.4	67	66.2	77.5	74.6	74.1	68	66.3

difference between the performances of daub4 and coif4, which are the wavelets of DWT; however, daub4 has been observed to perform slightly better. It has also been observed that KNN gives better results than SVM. The better recognition rate of KNN than SVM is consistent with the general studies conducted to recognize surface roughness in the literature [15,19,46,61]. In the study, the main purpose of performing recognition processes with CBS is to provide a way to show in which combination the manual performance of the system will reach the highest recognition rate. We wanted to understand how well the sensing tip tolerates errors in manual testing. As a result, it has been observed that there are minor differences between the recognition rates of the CBS and that of the manual test.

4. Conclusion

In this study, MHNT was used to identify the surface roughness based on the Fabry-Perot interferometer principle. Analog signals obtained from samples with different roughness levels with MHNT were subjected to a versatile test process. Sanding surfaces with roughness levels ranging from 6 μm to 269 μm were used. Test processes were evaluated in two main categories, CBS and manual, and in 16 categories in total. Feature vectors were found in two different ways using DWT's "coif4" and "daub4" wavelets. The test signals were classified with ML algorithms KNN and SVM using the feature vectors obtained with DWT. Thus, a total of 16 different categories were tested. The highest value for CBS (TWITD, daub4, KNN, and city block) was reached 84.2%. For Manual, the highest recognition rate (TWITD, daub4, KNN, and city block) was achieved as 80% with the combination. The TWOTD manual performance value was achieved as 77.5%.

Declaration of Competing Interest

The authors declare that they have no known competing financial interests or personal relationships that could have appeared to influence the work reported in this paper.

References

[1] P.G. Benardos, G.C. Vosniakos, Predicting surface roughness in machining: a review, Int. J. Mach. Tools Manuf. 43 (8) (2003) 833–844.

[2] K. Hsiao, P. Nangeroni, M. Huber, A. Saxena, A.Y. Ng, Reactive grasping using optical proximity sensors, in: Proceedings of the 2009 IEEE International Conference on Robotics and Automation, IEEE, May 2009, pp. 2098–2105.

[3] Y. Yamada, T. Morizono, Y. Umetani, H. Takahashi, Highly soft viscoelastic robot skin with a contact object-location-sensing capability, IEEE Trans. Ind. Electron. 52 (4) (2005) 960–968.

[4] W. Chen, H. Khamis, I. Birznieks, N.F. Lepora, S.J. Redmond, Tactile sensors for friction estimation and incipient slip detection—toward dexterous robotic manipulation: a review, IEEE Sens. J. 18 (22) (2018) 9049–9064.

[5] E. Choi, O. Sul, J. Lee, H. Seo, S. Kim, S. Yeom, S.B. Lee, Biomimetic tactile sensors with bilayer fingerprint ridges demonstrating texture recognition, Micromachines 10 (10) (2019) 642.

[6] M. Kaboli, R. Walker, G. Cheng, In-hand object recognition via texture properties with robotic hands, artificial skin, and novel tactile descriptors, in: Proceedings of 2015 IEEE-RAS 15th International Conference on Humanoid Robots (Humanoids), IEEE, November 2015, pp. 1155–1160.

[7] E. Kerr, T.M. McGinnity, S. Coleman, Material recognition using tactile sensing, Expert Syst. Appl. 94 (2018) 94–111.

[8] L. Jamone, L. Natale, G. Metta, G. Sandini, Highly sensitive soft tactile sensors for an anthropomorphic robotic hand, IEEE Sens. J. 15 (8) (2015) 4226–4233.

[9] H.R. Nicholls, M.H. Lee, A survey of robot tactile sensing technology, Int. J. Robot. Res. 8 (3) (1989) 3–30.

[10] G. Metta, G. Sandini, D. Vernon, L. Natale, F. Nori, The iCub humanoid robot: an open platform for research in embodied cognition, in: Proceedings of the 8th Workshop on Performance Metrics for Intelligent Systems, August 2008, pp. 50–56.

[11] P.A. Schmidt, E. Maël, R.P. Würtz, A sensor for dynamic tactile information with applications in human–robot interaction and object exploration, Robot. Auton. Syst. 54 (12) (2006) 1005–1014.

[12] G. Canavese, S. Stassi, C. Fallauto, S. Corbellini, V. Cauda, V. Camarchia, C.F. Pirri, Piezoresistive flexible composite for robotic tactile applications, Sens. Actuators A: Phys. 208 (2014) 1–9.

[13] C. Wang, D. Lv, H. Shi, X. Liu, R. Xin, Discussion on method of optical surface roughness measurement, in: Proceedings of Second International Conference on Photonics and Optical Engineering, International Society for Optics and Photonics, February 2017, vol. 10256, p. 1025654.

[14] A. Mohammadi, Y. Xu, Y. Tan, P. Choong, D. Oetomo, Magnetic-based soft tactile sensors with deformable continuous force transfer medium for resolving contact locations in robotic grasping and manipulation, Sensors 19 (22) (2019) 4925.

[15] Z. Yi, Y. Zhang, J. Peters, Bioinspired tactile sensor for surface roughness discrimination, Sens. Actuators A: Phys. 255 (2017) 46–53.

[16] A. Schmitz, P. Maiolino, M. Maggiali, L. Natale, G. Cannata, G. Metta, Methods and technologies for the implementation of large-scale robot tactile sensors, IEEE Trans. Robot. 27 (3) (2011) 389–400.

[17] L. Niu, M. Qian, W. Yang, L. Meng, Y. Xiao, K.K. Wong, H. Zheng, Surface roughness detection of arteries via texture analysis of ultrasound images for early diagnosis of atherosclerosis, PLoS One 8 (10) (2013) e76880.

[18] B. Luo, J. Zhang, X. Bao, H. Liu, L. Li, The effect of granularity on surface roughness and contact angle in wood sanding process, Measurement 165 (2020) 108133.

[19] C.M. Oddo, M. Controzzi, L. Beccai, C. Cipriani, M.C. Carrozza, Roughness encoding for discrimination of surfaces in artificial active-touch, IEEE Trans. Robot. 27 (3) (2011) 522–533.

[20] R. Windecker, H.J. Tiziani, Optical roughness measurements using extended white-light interferometry, Opt. Eng. 38 (6) (1999) 1081–1087.

[21] J. Schoenwald, A. Thiele, D. Gjellum, A novel fiber optic tactile array sensor, in: Proceedings of the 1987 IEEE International Conference on Robotics and Automation, IEEE, vol. 4, March 1987, pp. 1792–1797.

[22] H. Yamazaki, M. Nishiyama, K. Watanabe, A hemispheric hetero-core fiber optic tactile sensor for texture and hardness detection, in: Proceedings of Photonic Instrumentation Engineering III, International Society for Optics and Photonics, vol. 9754, March 2016, p. 97540X.

[23] H. Xie, H. Liu, S. Luo, L.D. Seneviratne, K. Althoefer, Fiber optics tactile array probe for tissue palpation during minimally invasive surgery, in: Proceedings of the 2013 IEEE/RSJ International Conference on Intelligent Robots and Systems, IEEE, November 2013, pp. 2539–2544.

[24] P. Kampmann, F. Kirchner, Integration of fiber-optic sensor arrays into a multimodal tactile sensor processing system for robotic end-effectors, Sensors 14 (4) (2014) 6854–6876.

[25] C. Bradley, J. Bohlmann, S. Kurada, A fiber optic sensor for surface roughness measurement, J. Manuf. Sci. Eng. (1998).

[26] J. Liu, K. Yamazaki, Y. Zhou, S. Matsumiya, A reflective fiber optic sensor for surface roughness in-process measurement, J. Manuf. Sci. Eng. 124 (3) (2002) 515–522.

[27] W. He, Computational neuroscience applied in surface roughness fiber optic sensor, Transl. Neurosci. 10 (1) (2019) 70–75.

[28] J.S. Heo, J.H. Chung, J.J. Lee, Tactile sensor arrays using fiber Bragg grating sensors, Sens. Actuators A: Phys. 126 (2) (2006) 312–327.

[29] Y.L. Park, K. Chau, R.J. Black, M.R. Cutkosky, Force sensing robot fingers using embedded fiber Bragg grating sensors and shape deposition manufacturing, in: Proceedings 2007 IEEE International Conference on Robotics and Automation, IEEE, April 2007, pp. 1510–1516.

[30] A.A. Abushagur, N. Arsad, M.I. Reaz, A. Bakar, Advances in bio-tactile sensors for minimally invasive surgery using the fibre Bragg grating force sensor technique: a survey, Sensors 14 (4) (2014) 6633–6665.

[31] C. Yan, E. Ferraris, T. Geernaert, F. Berghmans, D. Reynaerts, Characterisation of tactile sensors based on fibre Bragg gratings towards temperature independent pressure sensing, Procedia Eng. 47 (2012) 1402–1405.

[32] B.M. Cowie, D.J. Webb, B. Tam, P. Slack, P.N. Brett, Distributive tactile sensing using fibre Bragg grating sensors for biomedical applications, in: Proceedings of the First IEEE/RAS-EMBS International Conference on Biomedical Robotics and Biomechatronics, BioRob 2006, IEEE, February 2006, pp. 312–317.

[33] M.A. Qasaimeh, J. Dargahi, M. Kahrizi, M. Packirisamy, Design and analysis of tactile optical sensor for endovascular surgery, in: Photonics North, International Society for Optics and Photonics, vol. 6796, October 2007, p. 67960J.

[34] H. Su, M. Zervas, C. Furlong, G.S. Fischer, A miniature MRI-compatible fiber-optic force sensor utilizing fabry-perot interferometer, in: MEMS and Nanotechnology Springer, New York, NY, 2011, pp. 131–136.

[35] H. Su, M. Zervas, G.A. Cole, C. Furlong, G.S. Fischer, Real-time MRI-guided needle placement robot with integrated fiber optic force sensing, in: Proceedings of IEEE International Conference on Robotics and Automation, IEEE, May 2011, pp. 1583–1588.

[36] X. Liu, I.I. Iordachita, X. He, R.H. Taylor, J.U. Kang, Miniature fiber-optic force sensor based on low-coherence Fabry-Pérot interferometry for vitreoretinal microsurgery, Biomed. Opt. Express 3 (5) (2012) 1062–1076.

[37] Z. Wang, W. Zhang, J. Han, W. Huang, F. Li, Diaphragm-based fiber optic Fabry–Perot accelerometer with high consistency, J. Light. Technol. 32 (24) (2014) 4810–4815.

[38] M.P. Givens, Optical properties of metals, Solid State Phys. 6 (1958) 313–352.

[39] S.E. Hayber, T.E. Tabaru, S. Keser, O.G. Saracoglu, A simple, high sensitive fiber optic microphone based on cellulose triacetate diaphragm, J. Light. Technol. 36 (23) (2018) 5650–5655.

[40] X. Fu, P. Lu, J. Zhang, Z. Qu, W. Zhang, Y. Li, J. Zhang, Micromachined extrinsic Fabry-Pérot cavity for low-frequency acoustic wave sensing, Opt. Express 27 (17) (2019) 24300–24310.

[41] J. Choi, F. Cheng, J.W. Cleary, L. Sun, C.K. Dass, J.R. Hendrickson, X. Li, Optical dielectric constants of single crystalline silver films in the long wavelength range, Opt. Mater. Express 10 (2) (2020) 693–703.

[42] B. Josso, D.R. Burton, M.J. Lalor, Frequency normalised wavelet transform for surface roughness analysis and characterisation, Wear 252 (5–6) (2002) 491–500.
[43] S.J. Badashah, P. Subbaiah, Image enhancement and surface roughness with feature extraction using DWT, 2011.
[44] V. Niola, G. Nasti, G. Quaremba, A problem of emphasizing features of a surface roughness by means the Discrete Wavelet Transform, J. Mater. Process. Technol. 164 (2005) 1410–1415.
[45] M. Babič, M. Calì, I. Nazarenko, C. Fragassa, S. Ekinovic, M. Mihaliková, I. Belič, Surface roughness evaluation in hardened materials by pattern recognition using network theory, Int. J. Interact. Des. Manuf. (IJIDeM) 13 (1) (2019) 211–219.
[46] L. Qin, Y. Zhang, Roughness discrimination with bio-inspired tactile sensor manually sliding on polished surfaces, Sens. Actuators A: Phys. 279 (2018) 433–441.
[47] G. Tzanetakis, G. Essl, P. Cook, Audio analysis using the discrete wavelet transform, in: Proceedings of Conferences in Acoustics and Music Theory Applications, vol. 66, September 2001.
[48] M.Y. Gokhale, D.K. Khanduja, Time domain signal analysis using wavelet packet decomposition approach, Int. J. Commun. Netw. Syst. Sci. 3 (03) (2010) 321.
[49] S. Mallat, A Wavelet Tour of Signal Processing, Elsevier, 1999.
[50] R. Sharbati, F. Khoshnoudian, M. Koopialipoor, M.M. Tahir, Applying dual-tree complex discrete wavelet transform and gamma modulating function for simulation of ground motions, Eng. Comput. (2019) 1–17.
[51] L. Qin, Z. Yi, Y. Zhang, Enhanced surface roughness discrimination with optimized features from bio-inspired tactile sensor, Sens. Actuators A: Phys. 264 (2017) 133–140.
[52] P. Soucy, G.W. Mineau, A simple KNN algorithm for text categorization, in: Proceedings 2001 IEEE International Conference on Data Mining, IEEE, November 2001, pp. 647–648.
[53] T. Cover, P. Hart, Nearest neighbor pattern classification, IEEE Trans. Inf. Theory 13 (1) (1967) 21–27.
[54] V.S. Prasatha, H.A.A. Alfeilate, A.B. Hassanate, O. Lasassmehe, A.S. Tarawnehf, M. B. Alhasanatg, H.S.E. Salmane, Effects of distance measure choice on KNN classifier performance–a review, arXiv preprint arXiv:1708.04321, 2017.
[55] B. Samanta, K.R. Al-Balushi, S.A. Al-Araimi, Artificial neural networks and support vector machines with genetic algorithm for bearing fault detection, Eng. Appl. Artif. Intell. 16 (7–8) (2003) 657–665.
[56] S. Haykin, Neural networks and learning machines, 3/E. Pearson Education India, 2010.
[57] E. Jansons, J. Lungevics, K.A. Gross, Surface roughness measure that best correlates to ease of sliding, in: Proceedings of the International Scientific Conference, Latvia University of Agriculture, 2016.
[58] S.G. Mallat, A theory for multiresolution signal decomposition: the wavelet representation, IEEE Trans. Pattern Anal. Mach. Intell. 11 (7) (1989) 674–693.
[59] A. Subasi, M.I. Gursoy, EEG signal classification using PCA, ICA, LDA and support vector machines, Expert Syst. Appl. 37 (12) (2010) 8659–8666.
[60] R. Bajric, N. Zuber, G.A. Skrimpas, N. Mijatovic, Feature extraction using discrete wavelet transform for gear fault diagnosis of wind turbine gearbox, Shock Vib. (2016) 2016.
[61] J. Sinapov, V. Sukhoy, R. Sahai, A. Stoytchev, Vibrotactile recognition and categorization of surfaces by a humanoid robot, IEEE Trans. Robot. 27 (3) (2011) 488–497.

Serkan Keser received the M.S. and Ph.D. degrees from Eskişehir Osmangazi University, both in Electrical-Electronics Engineering, in 2008 and 2018, respectively. He is working as an Asst. Prof. at the Department of Electrical and Electronics Engineering, Kırşehir Ahi Evran University. His current research interests are signal and systems, digital signal processing, speech and image recognition, signal coding and artificial neural networks.

Sekip Esat Hayber received the M.S. and Ph.D. degrees in the Department of Electrical-Electronics Engineering from Erciyes University, Kayseri, Turkey, in 2011 and 2018, respectively. He is a full-time Asst. Prof. in the Department of Electrical and Electronics Engineering, Kırşehir Ahi Evran University, Turkey. His research involves optic and fiber optic detection, optical fiber sensing system, photonic sensors.